Generic path for droplet relaxation in microfluidic channels

P.-T. Brun, Mathias Nagel, and François Gallaire
Laboratory of Fluid Mechanics and Instabilities, EPFL, CH1015 Lausanne, Switzerland
(Received 27 March 2013; revised manuscript received 23 July 2013; published 22 October 2013)

In two-phase microfluidics, droplets often undergo deformations that drive them away from their circular equilibrium shape. Herein we concentrate on the relaxation of symmetrical deformations to a circle driven by surface tension effects, which are predominant at the micrometer scales. Working in a Hele-Shaw cell, we report a generic pathway for these types of relaxations. We simulate numerically the interface shape evolution and investigate it using linear stability analysis. Finally, we characterize this universal aspect of relaxation using a purely geometrical model that is tested in experiments.

DOI: 10.1103/PhysRevE.88.043009 PACS number(s): 47.61.Fg, 47.15.gp, 47.55.nb

I. INTRODUCTION

The strong interest in droplet-based microfluidics observed in recent years [1,2] is mostly underpinned by the promise of control offered when combining low Reynolds numbers, a tailorable geometry for channels, the predominance of surface tension effects, and the possibility to actuate them with external tweezers such as lasers. More fundamentally, this blooming field of science and industry relies on the capacity to form droplets of a fluid 1 and drive them at will using another immiscible fluid 2. An inherent consequence of such a methodology is that the droplet is often taken away from its equilibrium shape either when formed while breaking up [3]—from a jet or a bigger droplet—or instead when coalescing [4]. Similarly, deformations also arise when the droplet is trapped [5] or flows in a diverging (or converging) channel [6]. Such deformations have a limited lifetime. The predominance of surface tension effects at these scales eventually leads the deformed droplet to relax towards a more favorable geometry: a sphere or a circular pancake droplet depending on the channel confinement. Such relaxations have practical applications. In fact, the time scale of relaxation is directly related to the interfacial rheology that thereby may be measured [6]. Similarly, in the case of coalescence the resulting flows within the droplet and the bulk are of interest for applications that include chemical and biochemical reactions [7] since they rely on the mixing of different species. Thus droplet deformations are ubiquitous in two-phase microfluidics and are of practical interest. In addition, we will demonstrate that they have fundamental implications. Indeed, the confinement induced by the microchannel—when the droplet typical radius R outruns the channel height h—strongly impacts the flow [8] that will be seen to differ drastically from the thorough investigations on ellipsoidal drops relaxation in three-dimensional (3D) bulk flows [9,10].

II. RELAXATION OF AN ELLIPSE

Herein we report the study of an idealized, yet representative, case of relaxation: An initially flattened cylindrical droplet of fluid 1 with an elliptical cross section of area $\mathcal{A}$ is placed in a Hele-Shaw cell at $t = t_0$ where the surrounding fluid 2 is at rest [Fig. 1(a)]. The two fluids, of viscosity μ_1 and μ_2, are immiscible and subject to surface tension (denoted by γ) that drives the relaxation of the droplet at a typical speed $\tilde{v}$ obtained when balancing surface tension effects and viscous dissipation such that $\tilde{v}(\mu_1 + \mu_2) = \gamma$. Preferring $\mu_1 + \mu_2$ to μ_1 or μ_2 is quite arbitrary at this point and will be discussed later on. The investigation we propose is twofold. First, a numerical simulation for this ellipse is performed using an algorithm for dynamical problems in microfluidics [11]. Two questions that naturally arise when considering this problem are what the geometry of the relaxing droplet is and whether the droplet remains elliptic. Second, we tackle the relaxation analytically with a linear stability analysis that helps build a predictive reduced model of the dynamics as well as a geometric theory for droplets relaxation.

A. Nonmonotonic relaxation

At low Reynolds numbers the 3D Stokes equations prevail and can advantageously be averaged along the cell thickness h assuming $h \ll R$, where $R = \sqrt{\mathcal{A}/\pi}$ is the characteristic length of the problem ($\mathcal{A}$ is the area of the droplet). The resulting equations, called the Brinkman equations [12], are written

$$\eta_i(\triangle \boldsymbol{u}_j - k^2 \boldsymbol{u}_j) - \boldsymbol{\nabla} p_j = \boldsymbol{0}, \tag{1}$$

$$\boldsymbol{\nabla} \cdot \boldsymbol{u}_j = \boldsymbol{0}, \tag{2}$$

where $\boldsymbol{u}_j = u_j \boldsymbol{e}_r + v_j \boldsymbol{e}_\theta$ and p_j are, respectively, the fluid j dimensionless speed in the xy plane (expressed in polar coordinates) and dimensionless pressure field using $\tilde{v}$ and $\tilde{p} = \gamma/R$ as gauges. The parameters of this equation are $\eta_j = \mu_j/(\mu_1 + \mu_2)$ and $k = \sqrt{12}R/h$. Note that the differential operators and the variables are implicitly restricted to the cell plane and that we work with dimensionless variables. These equations go along with five scalar boundary conditions expressing (i) the impermeability of the interface, the continuity of both fluid (ii) normal and (iii) tangential speeds at the interface, (iv) the tangential stress continuity, and (v) the normal stress discontinuity, which can be written [13]

$$\boldsymbol{n} \cdot [\![\underline{\underline{\sigma}}]\!] \cdot \boldsymbol{n} = \gamma\left(\frac{\pi}{4}\kappa + \frac{2}{h}\right), \tag{3}$$

where κ denotes the in-plane curvature of the interface, $\underline{\underline{\sigma}}$ is the Cauchy stress tensor, $\boldsymbol{n}$ is the normal to the interface, and $[\![\cdot]\!]$ denotes a discontinuity.

Taking advantage of the predominance of interfaces in this problem, we use a boundary element method (BEM) [11] to solve this set of equations. The droplet interface $\partial\Omega$ is first discretized into the vertices $\boldsymbol{x}_i$. The classical BEM methodology [14] is followed with the exception of the choice

of the test velocity $\boldsymbol{w}$ and the test stress $\underline{\underline{\tau}}$ that are relevant to the Brinkman equation. In the present case these Green's functions solve

$$\nabla \cdot \underline{\underline{\tau}} - k^2 \boldsymbol{w} = \delta(\boldsymbol{x_i})\boldsymbol{e}_j, \quad \nabla \cdot \boldsymbol{w} = 0, \tag{4}$$

where $\delta(\boldsymbol{x_i})$ denotes the Dirac distribution centered on a mesh vertex $\boldsymbol{x_i}$ lying on $\partial\Omega$ and $\boldsymbol{e}_j$ may point in the x or y direction. At each time step these functions help building a linear algebraic system linking the vertex velocities $\boldsymbol{v}_i(t)$ to the interfacial stress jump given by (3). Additionally, the interface motion is ensured by an implicit time marching algorithm solving $\dot{\boldsymbol{x}}_i = \boldsymbol{v}_i$, where the overdot denotes the time derivative.

Note that the surface tension γ actually sets the time scale $\tilde{t} = R(\mu_1 + \mu_2)/\gamma$ of this evolution, but does not affect the successive shapes of the interface. They solely depend on the two parameters: η_1 and k (or equivalently $\eta_2 = 1 - \eta_1$ and k). Given the generalized Laplace law for the normal stress jump (3) at the interface, we anticipate that the planar geometry of the interface parametrized by its arclength $\boldsymbol{r}(s)$ and the interface curvature $|\boldsymbol{r}_{,ss}| = \kappa$ are of interest in this study. In particular, we define the south and east curvatures denoted $\kappa_s = \kappa(0)$ and $\kappa_e = \kappa(\mathcal{P}/4)$, respectively, where $\mathcal{P}$ is the flattened drop perimeter [Fig. 1(a)].

Without loss of generality, we consider the relaxation of elliptic droplets of area $\mathcal{A} = \pi$ (i.e., $R = 1$ and all variables are dimensionless) that have a different initial deformation $D_f(t = 0)$, where $D_f = (L - W)/W$ denotes the deformation coefficient and L and W are the drop length and width, respectively [see Fig. 1(a)]. As a first step both viscosities are assumed equal ($\eta_1 = 1/2$) and the dimensionless height of the channel is chosen to be $h = \frac{1}{4}$, a typical value for microfluidic systems yielding $k = 8\sqrt{3} \simeq 13.86$, a sufficiently large value for the depth-averaged model to be accurate [12]. Shown in Fig. 1 is the relaxation diagram of three elliptic droplets obtained with our BEM.[1] As for perimeters [Fig. 1(d)], they all monotonically relax towards the value of 2π that corresponds to the perimeter of a circle of curvature $\kappa = 1$ minimizing $\mathcal{P}$, and thus the surface energy, for a given area $\mathcal{A}$. Here $\mathcal{A}$ may be interpreted as the droplet volume in our depth-averaged formalism. Unlike $\mathcal{P}$, some other variable evolutions are nonmonotonic and are of particular interest for the rest of this article.

In the following, the droplet's path of relaxation is described in terms of curvature. Ellipses verify the relation $\kappa_s = 1/\kappa_e$. Therefore, they fall on the curve $1/\kappa_s + \kappa_s$ in the parameter space $(\kappa_e + \kappa_s, \kappa_s)$ and thus the $t = t_0$ extremities of the three relaxation trajectories are found on that very curve. One could expect these ellipses to relax while remaining elliptic [15], i.e., to follow the dotted line in Fig. 1(b). On the contrary, the heel-shaped relaxation curves as well as the successive shapes of the droplets reported in Fig. 1 strongly suggest a different and nonmonotonic scenario. This scenario is depicted in the case of ellipse a verifying $D_f(0) = 8$. Shown in Fig. 1(c) is the superimposition of the time t_0 and the time t_1, where one

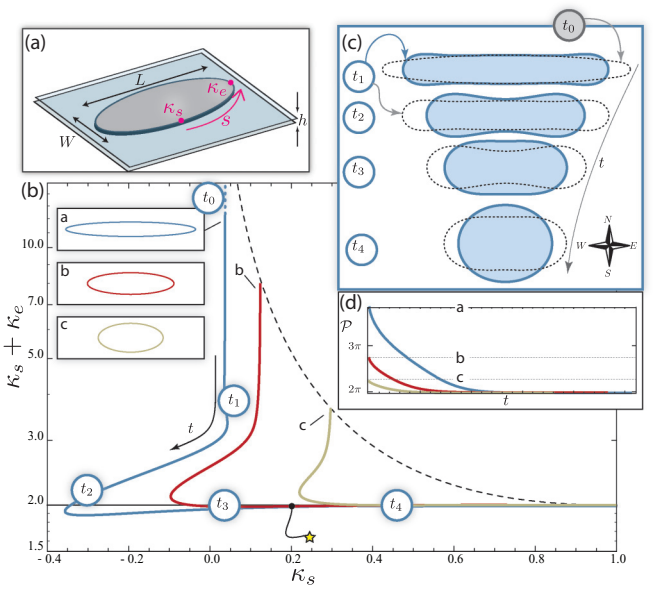

FIG. 1. (Color online) (a) Idealized case study. An elliptical droplet of typical size R and initial deformation $D_f = \frac{L-W}{W}$ is placed in a Hele-Shaw cell of height $h \ll R$. (b) Relaxation pathways in the plane $(\kappa_n + \kappa_e, \kappa_n)$ corresponding to the ellipses of initial deformations $D_f = 8$, 3, and 5/4 (curves a, b, and c, respectively). (c) Time evolution of the drop interface for $D_f = 8$ (solid lines). At $t = t_i$ the dotted line recalls the drop at $t = t_{i-1}$. (d) Perimeter as a function of time in each case.

may observe that the most curved parts of the ellipse (east and west) initiate their relaxation while the least curved parts (south and north) remain motionless. As a consequence, κ_e decreases while κ_s remains constant and the relaxation curve decreases vertically. The inflections of the interface induced by the east and west parts of the respective relaxations then reach the north and south poles and cause the curvature there to decrease and possibly change sign (at $t = t_2$ for ellipse a). This is responsible for the heel-like shape of these relaxation curves. Of particular interest is the third and last part of relaxation in which the droplets then enter. Remarkably, all relaxation curves eventually collapse on a master curve defined by

$$\kappa_e + \kappa_s = 2 \tag{5}$$

(this event occurs at $t = t^\star$ and is marked by a star in Fig. 1 for ellipse a). It is crucial to note that the value 2 is reached before the relaxation is complete (that is, when $D_f = 0$). Therefore, from $t^\star$ onward both curvatures trade for each other; their evolutions balance each other while their sum remains constant and equal to 2. Everything happens as if the curvature was flowing from areas of excess (east and west) to deprived areas (north and south). A quantitative analysis of such a relaxation is reported next and is generalized to different aspect ratios k as well as different viscosity ratios η_1.

B. Quantitative analysis of relaxation

Shown in Fig. 2(a) is the time evolution of the deformation $D_f(t)$ for different aspect ratios $4 \leqslant R/h \leqslant 10$ and $\eta_1 = 1/2$ in the case of ellipse c [$D_f(0) = 5/4$; see Fig. 1]. After the earlier described initial stage of relaxation the deformations

[1] In a typical run, such as the one for $D_f(0) = 3$, 347 points are used to discretize the interface so that the discretization is $ds \simeq 0.01 = dt$. The run lasts 4 min 49.4 sec on a 2.6-GHz processor with 8 Go of RAM.

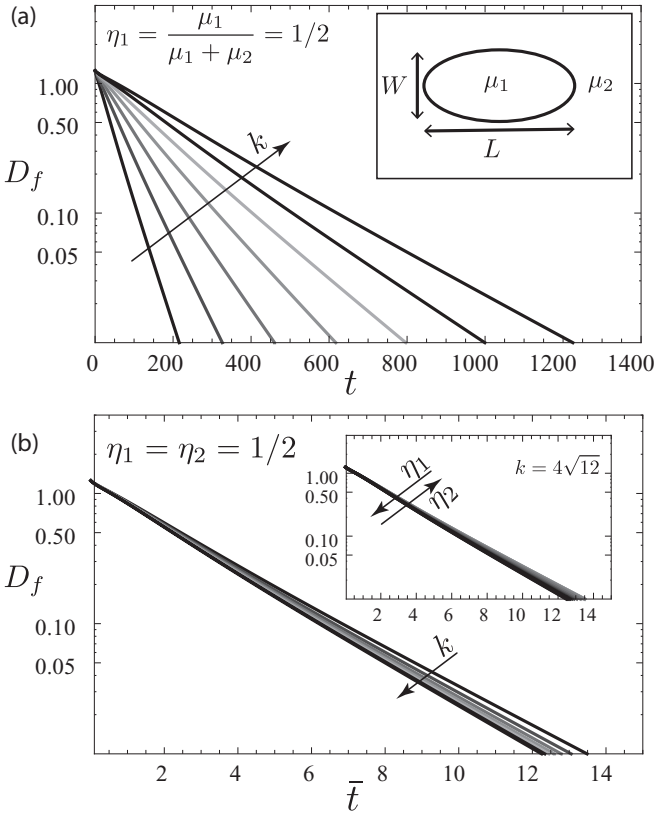

FIG. 2. (a) Deformation coefficient $D_f = (L - W)/W$ as a function of the time t for several values of $k = \sqrt{12}\frac{R}{h}$ ($4\sqrt{12} \leqslant k \leqslant 10\sqrt{12}$) and $\eta_1 = 1/2$. (b) The same data plotted as a function of $\bar{t}$ shows a collapse. The inset shows that a similar collapse is possible when varying η_1 while k is fixed ($0 \leqslant \eta_1 \leqslant 10/11$).

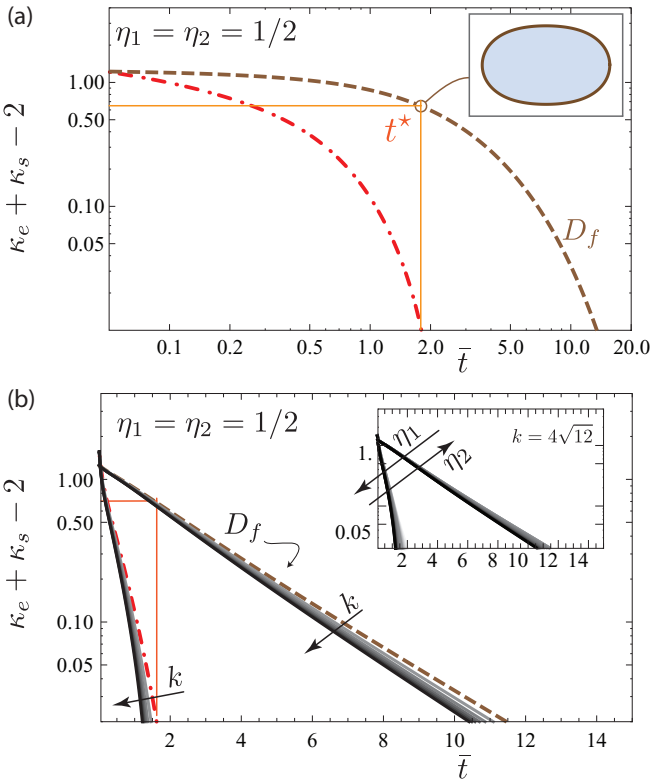

FIG. 3. (Color online) (a) Convergence of $\kappa_s + \kappa_e$ towards 2 for $\eta_1 = 1/2$ and $k = 4\sqrt{12}$ (dash-dotted line). Here $t^\star$ is the time when the sum of curvatures has converged with 0.05% error. Note that $t^\star \sim 2$ is much smaller than the time needed for the droplet to become almost circular ($\bar{t} \sim 15$) (the dashed curve represents the deformation). The inset shows the droplet at $t^\star$. (b) Generalization of (a) varying k and showing the collapse obtained with $\bar{t}$ in lin-log coordinates. The inset shows that a similar collapse is possible when varying η_1 while k is fixed ($0 \leqslant \eta_1 \leqslant 10/11$).

appear to be exponentially decreasing. Note that the overall time of relaxation is an increasing function of the ratio R/h (and thus k) as explained next.

The relaxation is driven by surface tension effects that induce a pressure field scaling as $\gamma(\frac{2}{h} + \frac{\pi}{4R})$ [13], where $\frac{1}{R}$ is the typical in-plane curvature of the droplet. This pressure term is dominated by the factor $\frac{2}{h}$ as we consider a confined environment ($h \ll R$). However, this term is fixed by the channel geometry. Consequently, only the in-plane curvature is meant to evolve while the droplet relaxes. A proper evaluation of the active term of the pressure field imposed by surface tension is therefore γ/R. This driving mechanism is counterbalanced by the viscous damping, itself dominated by terms in the normal direction yielding to $\mu\bar{v}/h^2 \sim \frac{1}{R}\gamma/R$, where $\bar{v}$ is the yet undermined characteristic velocity and $\mu = \mu_1 + \mu_2$ is a typical viscosity. Note that the extra $\frac{1}{R}$ on the right-hand side denotes the gradient of the pressure field. One eventually obtains

$$\bar{v} = \frac{\gamma}{\mu}\frac{h^2}{R^2} = \tilde{v}\frac{h^2}{R^2}, \tag{6}$$

where $\tilde{v}$ is the first speed gauge established earlier in the Introduction that was built on the classical construction of the capillary number. Equation (6) suggests the rescaling $\bar{t} = t\frac{h^2}{R^2}$ that leads to the collapse of the relaxation plots in Fig. 2(b). Note that the use of $\mu = \mu_1 + \mu_2$ as a viscosity gauge is consistent, as shown by the collapse in the inset of Fig. 2(b) obtained when varying η_1.

We now concentrate on the axial curvatures κ_s and κ_e and in particular compare their evolutions to the one of the deformation $D_f(\bar{t})$. As the ellipse relaxes towards a circle it is obvious that κ_s and κ_e both tend to 1. However, their sum $\kappa_s + \kappa_e$ and especially its deviation to the value 2 are now investigated for $R/h = 4$, with equally viscous fluids and $D_f(0) = 5/4$ (Fig. 3). The convergence of $\kappa_s + \kappa_e$ towards 2 is ensured (with an error of 0.05%) at a time denoted $t^\star$, while the deformation is still large $D_f \simeq 0.7$ (inset of Fig. 3). For $\bar{t} > t^\star$ the droplet relaxes while the sum of its south and east curvature is conserved and their respective evolutions balance each other (κ_s is increasing and κ_e decreasing). This result is remarkably general in the sense that it does not depend on either k or η_1, as shown by the collapses in Fig. 3(b). We now derive a model to shed light on the earlier reported observations.

III. TWO COMPLEMENTARY MODELS FOR RELAXATION

A. Linear model

To explain the vertical part of the curvature relaxation trajectories reported above, that is, to explain why ellipses

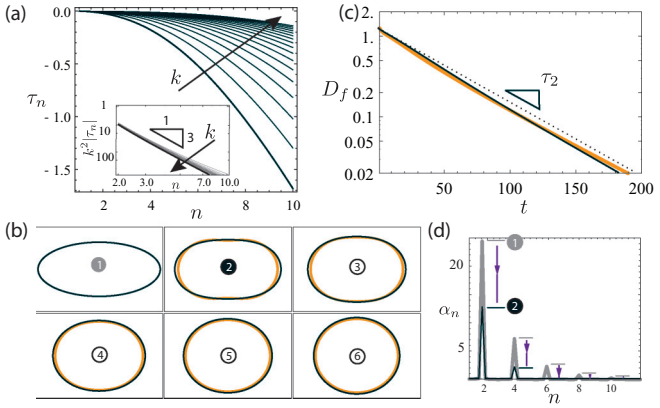

FIG. 4. (Color online) (a) Shown is $\tau_n(n)$ for increasing values of k. (b) Superposition of relaxation shapes calculated by the BEM (black) and the one obtained with the linear stability analysis [gray (orange)] for $k = 4\sqrt{12}$. (c) Plot of the deformation D_f shown for the BEM (in black) and the linear stability analysis [gray (orange)], respectively. The dotted line is the result found with one mode only. (d) Fast Fourier transform of the oscillating part of $\kappa(\theta)$ corresponding to the states denoted by 1 and 2, respectively.

do not remain as such while relaxing, we proceed with a linear analysis. We consider a weak elliptical deformation of a circle ($D_f \ll 1$). Over time this ellipse relaxes and is written $r(\theta,t) = \alpha_0 + \sum_{n\geqslant 1} \epsilon\alpha_n(t)\cos(n\theta)$ in polar coordinates using a cosine Fourier decomposition where $\epsilon \ll 1$ and the values of α_0 and $\alpha_n(0) = \alpha_n^0$ for $n \in \mathbb{N}^+$ are chosen to match the initial shape of the ellipse. The time evolution is assumed to be $\alpha_n(t) = \alpha_n^0 \exp(\tau_n t)$. The values of τ_n, which may be complex, are obtained through a linear stability analysis, which we now briefly outline. A complex stream function Ψ_j is introduced for each fluid j. In polar coordinates they relate to the speed $\boldsymbol{u}_j$ through the relation $\boldsymbol{u}_j = \frac{1}{r}\frac{\partial\Psi_j}{\partial\theta}\boldsymbol{e_r} - \frac{\partial\Psi_j}{\partial r}\boldsymbol{e_\theta}$ and may be expressed in a generic form [16]

$$\Psi_1(r,\theta) = \mathbf{i}\left(a_n\frac{I_n(kr)}{I_n(k)} + b_n r^n\right)\exp \mathbf{i}n\theta, \tag{7}$$

$$\Psi_2(r,\theta) = \mathbf{i}\left(c_n\frac{K_n(kr)}{K_n(k)} + d_n r^{-n}\right)\exp \mathbf{i}n\theta, \tag{8}$$

where I_n and K_n denote the nth Bessel I and K functions, respectively,[2] and a_n, b_n, c_n, and d_n are coefficients that are yet to be determined. The boundary conditions (i)–(v) expressed earlier (see Sec. II A) may be rewritten using these stream functions and form a linear problem

$$\underline{\underline{M}}(\tau_n)\cdot\mathcal{V} = \mathbf{0}, \tag{9}$$

where $\mathcal{V} = (a_n,b_n,c_n,d_n,\alpha_n^0)$ and $\underline{\underline{M}}$ may be seen as the impedance of the system. Nontrivial solutions are found only if $\det[\underline{\underline{M}}(\tau_n)] = 0$. Shown in Fig. 4(a) is a plot of the corresponding values of τ_n for different values of k in the case of equally viscous fluids. Note that these values are all negative real numbers, thus no instability arises. More important is that the higher the mode, the faster its decrease, as pointed out by the negative slope of the curves. This will prove to have a large impact on the dynamics of relaxation as explained later. Let us first point out that from the exact solution of (9) one may derive the scaling law $\tau_n \sim -\frac{n(n^2-1)\pi}{4k^2}$ for large values of k [see the inset in Fig. 4(a)]. Note that this scaling is independent of the viscosity ratio and therefore confirms that the choice of $\mu_1 + \mu_2$ as a viscosity gauge is consistent. It also explains why the earlier proposed scaling $\bar{t} = th^2/R^2$ provided a collapse in Figs. 2 and 3 (since $\tau_n \propto h^2/R^2$).

The modes τ_n obtained earlier are now used to model the dynamics of relaxation of the ellipse such that $r(\theta,t) = \alpha_0 + \sum_{n\geqslant 1}\alpha_n^0\exp(\tau_n t)\cos(n\theta)$. Shown in Fig. 4(c) is the time evolution of the deformation coefficient $D_f(t)$ for this model as well as the one obtained with our BEM for ellipse c. Even for such a reasonably large initial deformation the agreement between the full calculation and the linear model remains acceptable [Figs. 4(b) and 4(c)]. Note that symmetry is conserved over time while the ellipse relaxes towards a circle. Note also that the volume conservation is only granted in the linear approximation yielding $\alpha_0 = 1 - O(\epsilon^2)$ for ellipses of area π. Consequently, the final shape predicted by the model in Fig. 4(b) has a radius α_0 slightly smaller than 1.

Differentiating the previous expression for $r(\theta,t)$, one finds that the linearized curvature Fourier modes scale as $(n^2-1)\alpha_n^0\exp\tau_n t$. Therefore, the higher a Fourier mode of the curvature the more it is damped. Shown in Fig. 4(d) are the fast Fourier transform spectra of the oscillating part of the curvature $\kappa(\theta)$ computed at two different times with our BEM and corresponding to the interfaces denoted by 1 and 2 in Fig. 4(b). As suggested by the analysis, the highest modes vanish in the time interval between the two shots. Consequently, only two low-order peaks remain after some time and this type of spectrum does not coincide with the one of an ellipse. On the contrary, they correspond to a family of ovals that we introduce next.

B. The κ_2 ovals

A geometrical model for the droplet relaxation shapes is developed below using the relation (5). The modeled shapes are coined κ_2 ovals after Eq. (5). They additionally follow some more conventional geometrical constraints, namely, (i) the periodicity ensuring a closed interface, (ii) the symmetry along both Cartesian axes, and (iii) the conservation of the droplet volume $\mathcal{A}$. Building upon the linear analysis results and (i) we propose the following ansatz for the droplet curvature profile: $\kappa(s) = a - b\cos(\frac{4\pi}{\mathcal{P}}s) - c\cos(2\frac{4\pi}{\mathcal{P}}s)$, where $\mathcal{P}$ is the drop perimeter, s is the interface arc length, and the minus signs help anticipate the inequality $\kappa_s \leqslant \kappa_e$. Note that four degrees of freedom (a, b, c, and $\mathcal{P}$) are *a priori* necessary to satisfy the four stated geometrical constraints. Applying (5) and (ii) leads to $\kappa(s) = \frac{1}{\mathcal{P}}[2\pi - b\mathcal{P}\cos(\frac{4\pi}{\mathcal{P}}s) + (\mathcal{P}-2\pi)\cos(\frac{8\pi}{\mathcal{P}}s)]$ and leaves two parameters in the model: the perimeter $\mathcal{P}$ and b, which may be interpreted as a coefficient of deformation. These two parameters are actually tied together by the remaining constraint (iii), which is written $\mathcal{A} = \frac{1}{2}\int xy' - yx' = \pi$ in Cartesian coordinates. This relation explicitly depends on the shape of the drop that

[2]Here $I_n(r)$ is solution of $r^2y'' + ry' - (r^2+n^2)y = 0$ and $K_n(r)$ of $r^2y'' + ry' - (r^2+n^2)y = 0$.

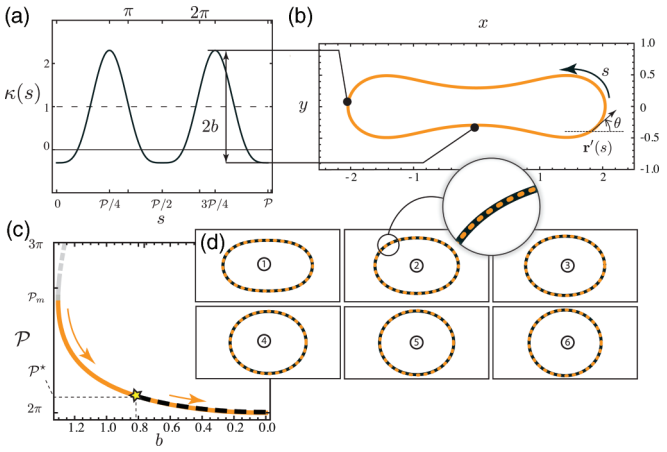

FIG. 5. (Color online) (a) Plot of the ansatz of the curvature in the particular case of the κ_2 oval shown in (b). (c) Relation between the two parameters $\mathcal{P}$ and b that characterize the κ_2 ovals. The light gray is the unphysical part and the gray (orange) is the κ_2 branch compared to the simulation results (dotted black). (d) Comparison between the full BEM numerical simulation (black) with the corresponding κ_2 ovals in dotted gray (orange) lines.

we integrate with a numerical shooting method solving the system:

$$\left(\frac{d\theta}{ds},\frac{dx}{ds},\frac{dy}{ds}\right) = [\kappa(s),\cos\theta(s),\sin\theta(s)], \tag{10}$$

$$[\theta(0),x(0),y(0)] = (0,0,0), \tag{11}$$

where the main unknown is the position of the droplet interface (x,y) reconstructed from θ, which tracks the orientation of the tangent to its interface. The unknowns b and $\mathcal{P}$ (both found in the expression of κ) are the shooting parameters. The recovered interface is centered around the origin after integration. A typical result and the corresponding curvature function are displayed in Figs. 5(a) and 5(b). This solution is not unique; there is a 1D family of such ovals that may be represented in the parameters plane $(\mathcal{P},b)$. The branch for which the perimeter is an increasing function of the deformation $(\partial\mathcal{P}/\partial b > 0)$ is shown in Fig. 5(c) [dark gray (orange)]. This curve describes the so-called κ_2 oval family.

These ovals, solely obtained with geometrical considerations, are now compared to the shapes found when solving the full dynamics of relaxation (the BEM) for $t > t^\star$, that is, when the droplets verify (5). Some of the BEM shapes are shown in Fig. 5(d) (black) working with the ellipse of initial deformation $D_f = 8$ (denoted a in Fig. 1). For each BEM shape, the easternmost position of the interface is used to select the corresponding κ_2 oval among the family obtained earlier so that no adjustable parameter is used. This κ_2 oval is plotted for comparison in Fig. 5(d) [dashed gray (orange) line] and the agreement is excellent. Consequently, under a certain level of deformation (corresponding to a perimeter $\mathcal{P}^\star$ and the time $t^\star$) the droplet continuously explores the κ_2 oval family while relaxing towards the limiting circle [as shown in Fig. 5(c)]. Similar results are obtained when investigating ellipses of different eccentricities that lead to diverse values of $\mathcal{P}^\star$. Since the branch $\mathcal{P}(b)$ has a turning point, the existence of an upper bound for the matching point between the relaxation shapes and the κ_2 ovals is anticipated, yielding $\mathcal{P}^\star < \mathcal{P}_m$, where $\mathcal{P}_m$ is the fold point of the solutions family shown in Fig. 5(c). We show in the following discussion that these results are not limited to ellipses, but extend to broader cases.

IV. DISCUSSION

As explained earlier, the occurrence of κ_2 ovals is supported by the fast damping of high-order deformation modes that keeps the lower ones afloat. Therefore, this type of result may apply to other symmetrical shapes relaxing to a circle. To illustrate this generic aspect we explore a different and ubiquitous type of relaxation: the coalescence of two identical droplets of area $\mathcal{A}_i = \pi/2$.

This coalescence is achieved experimentally in polydimethylsiloxane microchannels fabricated using a silicon wafer that has been etched with soft lithography methods and then bonded by plasma to a glass slide. Water is used as the external phase and fluorinated oil (FC40) as a dispersed phase. Both liquids are injected via syringe pumps (cetoni Nemesys) into the chip. The microchannel of height $h = 25$ μm consists of a cross junction followed by a straight channel of width of 160 μm. Far from the cross junction used to shed droplets the channel width then increases linearly to reach 600 μm, where coalescence by separation is performed [4]. A typical sequence observed with a Zeiss AxioVert A.1 microscope coupled to a Miro M310 high-speed camera is shown in Fig. 6.

The early times of coalescence are a 3D phenomenon [4,17,18] that we do not attempt to solve here. Instead, we consider the configuration at $t = 0^+$ shown in Fig. 6 as a starting point for our simulations. As inferred from the velocity map in Fig. 6, only the most curved parts of the interface relax initially (that is, κ_e). The dimensionless speed of the interface at these points is about 40 times greater than anywhere else. The droplet relaxes going through a wealth of shapes such as a peanutlike shape, racetracks, and ovals, and ends up circular. These shapes are accurately recovered by our numerical simulations, as seen in Fig. 6. Remarkably, as soon as the sum of both curvatures

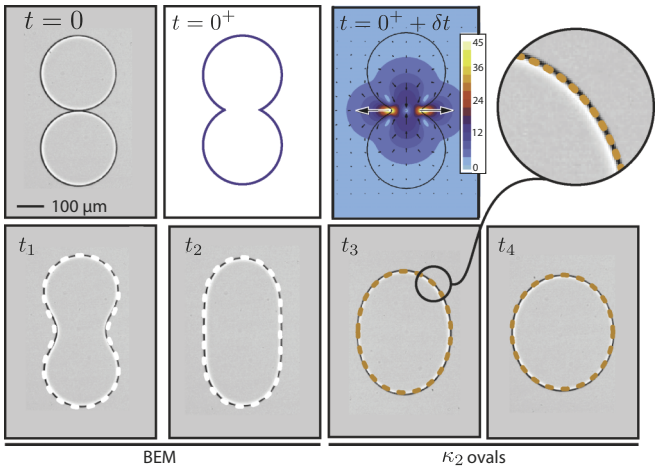

FIG. 6. (Color online) Two droplets before coalescence ($t = 0$) and the initial configuration used in our numerically investigation ($t = 0^+$); velocity map of the droplet at $t = 0^+ + \delta t$; and comparison with experimental pictures: BEM shapes (dashed white) and κ_2 ovals [dashed gray (orange)] at $t = 0.18$, 1.57, 7.15, and 13.63 ms.

verifies (5), the droplet enters a final stage of relaxation where both curvatures evolve while satisfying the κ_2 oval criterion. A comparison between experimental pictures and the κ_2 ovals is provided as an illustration and shows very good agreement.

Note that the κ_2 ovals, found here after coalescence, are generic. They will appear as soon as an initially symmetrical form relaxes to a circle. Indeed, their presence is ensured by a faster damping of higher modes of deformations and this is always true for relaxing droplets in a confined environment.

V. CONCLUSION

In summary, we have considered the relaxation of symmetrically shaped droplets in Hele-Shaw cells and have found a generic behavior. In contrast with what classically occurs in 3D bulk flows, the droplet shapes are attracted by a family of ovals, which verify Eq. (5). These κ_2 ovals are then constructed geometrically and are of valuable help in predicting the interface shapes and flows in diverse events such as coalescence. Future work will consist in exploring the $\mathcal{P}(b)$ folding point as well as investigating the optimality of this area-preserving and perimeter-shortening motion reminiscent of the Mullins-Sekerka problem [19] and its finite-time singularities [20].

ACKNOWLEDGMENT

We thank P. Renaud for hosting our experiments in his laboratory. This work was supported by the ERC SIMCOMICS (No. 280117).

[1] T. Beatus, R. H. Bar-Ziv, and T. Tlusty, Phys. Rep. **516**, 103 (2012).
[2] C. N. Baroud, F. Gallaire, and R. Dangla, Lab Chip **10**, 2032 (2010).
[3] D. R. Link, S. L. Anna, D. A. Weitz, and H. A. Stone, Phys. Rev. Lett. **92**, 054503 (2004).
[4] N. Bremond, A. R. Thiam, and J. Bibette, Phys. Rev. Lett. **100**, 024501 (2008).
[5] R. Dangla, S. Lee, and C. N. Baroud, Phys. Rev. Lett. **107**, 124501 (2011).
[6] S. D. Hudson, J. T. Cabral, W. J. Goodrum, K. L. Beers, and E. J. Amis, Appl. Phys. Lett. **87**, 081905 (2005).
[7] T. Squires and S. Quake, Rev. Mod. Phys. **77**, 977 (2005).
[8] P. J. A. Janssen and P. D. Anderson, Phys. Fluids **19**, 043602 (2007).
[9] H. A. Stone, Annu. Rev. Fluid Mech. **26**, 65 (1994).
[10] L. G. Leal, *Advanced Transport Phenomena: Fluid Mechanics and Convective Transport Processes* (Cambridge University Press, Cambridge, 2007).
[11] M. Nagel and F. Gallaire, Bull. Am. Phys. Soc. **57**, 17 (2012).
[12] W. Boos and A. Thess, J. Fluid Mech. **352**, 305 (1997).
[13] C.-W. Park and G. M. Homsy, J. Fluid Mech. **139**, 291 (1984).
[14] C. Pozrikidis, *Boundary Integral and Singularity Methods for Linearized Viscous Flow* (University of Cambridge Press, Cambridge, 1992).
[15] G. Taylor and P. G. Saffman, Q. J. Mech. Appl. Math. **12**, 265 (1959).
[16] F. Gallaire, P. Laure, P. Meliga, and C. N. Baroud (unpublished).
[17] J. Eggers, J. R. Lister, and H. A. Stone, J. Fluid Mech. **401**, 293 (1999).
[18] M. Yokota and K. Okumura, Proc. Natl. Acad. Sci. USA **108**, 6395 (2011).
[19] U. F. Mayer, Electron. J. Diff. Eqs. **1**, 171 (1997).
[20] R. Almgren, Phys. Fluids **8**, 344 (1996).